# Emergence of Bimodal Motility in Active Droplets

Babak Vajdi Hokmabad[1], Ranabir Dey[1,2], Maziyar Jalaal[3,4,5], Devaditya Mohanty[6]
Madina Almukambetova[7], Kyle A. Baldwin[1,8], Detlef Lohse[3], and Corinna C. Maass[1,3,*]

[1]*Max Planck Institute for Dynamics and Self-Organization and Institute for the Dynamics of Complex Systems, Georg August Universität Göttingen, 37077 Göttingen, Germany*
[2]*Department of Mechanical and Aerospace Engineering, Indian Institute of Technology Hyderabad, Kandi, Sangareddy, Telengana 502285, India*
[3]*Physics of Fluids Group, Max Planck Center for Complex Fluid Dynamics, MESA+Institute and J. M. Burgers Center for Fluid Dynamics, University of Twente, P.O. Box 217,7500 AE Enschede, Netherlands*
[4]*Department of Applied Mathematics and Theoretical Physics, University of Cambridge, Cambridge CB3 0WA, United Kingdom*
[5]*Van der Waals-Zeeman Institute, Institute of Physics, University of Amsterdam, PO box 94485, 1090 GL Amsterdam, Netherlands*
[6]*Indian Institute of Technology Guwahati, Assam 781039, India*
[7]*Ulsan National Institute of Science and Technology (UNIST), Ulsan 44919, Republic of Korea*
[8]*SOFT group, School of Science and Technology, Nottingham Trent University, Nottingham, NG11 8NS, United Kingdom*

Artificial model swimmers offer a platform to explore the physical principles enabling biological complexity, for example, multigait motility: a strategy employed by many biomicroswimmers to explore and react to changes in their environment. Here, we report bimodal motility in autophoretic droplet swimmers, driven by characteristic interfacial flow patterns for each propulsive mode. We demonstrate a dynamical transition from quasiballistic to bimodal chaotic propulsion by controlling the viscosity of the environment. To elucidate the physical mechanism of this transition, we simultaneously visualize hydrodynamic and chemical fields and interpret these observations by quantitative comparison to established advection-diffusion models. We show that, with increasing viscosity, higher hydrodynamic modes become excitable and the droplet recurrently switches between two dominant modes due to interactions with the self-generated chemical gradients. This type of self-interaction promotes self-avoiding walks mimicking examples of efficient spatial exploration strategies observed in nature.

## I. INTRODUCTION

In response to physical constraints in nature, microorganisms have adapted and developed various locomotion strategies. Depending on cues from the environment, these strategies range from the more commonplace helical swimming [1,2], run-and-tumble, and switch-and-flick motility [3] to more sophisticated transient behaviors, e.g., peritrichous bacteria switching poles in response to

a steric stress [4], octoflagellate microalgae exhibiting run-stop-shock motility with enhanced mechanosensitivity [5], and starfish larvae maximizing fluid mixing, and thereby nutrition uptake, through rapid changes of ciliary beating patterns [6]. Such intricate gait-switching dynamics [7,8] enable organisms to navigate in external flows [9,10], to follow gradients [11], or to efficiently explore their environment [12,13]. Recent efforts in the development of synthetic swimmers have led to the synthesis of systems that are capable of mimicking some of the aforementioned features of their natural counterparts such as rheotaxis [14,15], chemotaxis [16,17], and gravitaxis [18]. However, dynamic multimodal motility in the absence of external actuation has not been explored before in artificial swimmers, and the mechanisms underlying unsteady behavior in self-actuating systems are not well understood, particularly with respect to distinguishing states with

increased random fluctuation from ones featuring true multimodal behavior [19,20].

Paradigms for biomimetic artificial swimmers include autophoretic microswimmers, powered by chemical activity at their interface, which are able to generate long-living chemical gradients in the environment [17]. In this regard, droplet microswimmers driven by micellar solubilization [21] provide a sophisticated experimental realization. Unlike most synthetic swimmers which are inherently asymmetric, active droplets are isotropic. Interfacial activity spontaneously breaks the symmetry, allowing for the emergence of different flow patterns depending on the environmental parameters. Here, we use such active droplets as model systems to demonstrate the physical principles guiding the emergence of multimodal motility in response to changes in environmental conditions.

We show that active droplets adapt to an increase in the viscosity of the swimming medium by exhibiting increasingly chaotic motion—a counterintuitive response given that increasing viscous stress generally tends to stabilize noninertial dynamics. Using time-resolved *in situ* visualization of the chemical and the hydrodynamic fields around the droplet interface, we find that the emergence of the chaotic dynamics correlates with the onset of higher hydrodynamic modes at increasing Péclet number Pe. Once these higher modes prevail, the droplet exhibits an unsteady bimodal exploration of space triggered by its interaction with a self-generated, slowly decaying chemical gradient. The conditions for the onset of this dynamical transition are quantitatively predicted by an advection-diffusion model for the transport of the chemical species, which takes into account the nonlinear coupling between the hydrodynamic and chemical fields. The visualization technique and the findings presented here lay the groundwork for future investigations of emergent dynamics in active phoretic matter.

## II. DROPLETS PROPELLED BY MICELLAR SOLUBILIZATION

Our experiments use a specific subclass of active droplets: oil droplets that are slowly dissolving in supramicellar aqueous solutions of ionic surfactants. The droplets spontaneously develop self-sustaining gradients in interfacial surfactant coverage, resulting in Marangoni stresses which lead to self-propulsion [22]. This interfacial instability may be understood as follows [Figs. 1(a) and 1(b)]: During the solubilization of the droplet, oil molecules migrate into surfactant micelles in a boundary layer around the droplet interface, causing the micelles to swell and take up additional surfactant monomers from the aqueous phase, therefore reducing the local density of monomers $c$ below its equilibrium, the critical micelle concentration (CMC). Unless there are empty micelles present to restore the CMC by disintegration, this local mismatch reduces the interfacial surfactant coverage, such that the interfacial tension increases with the local
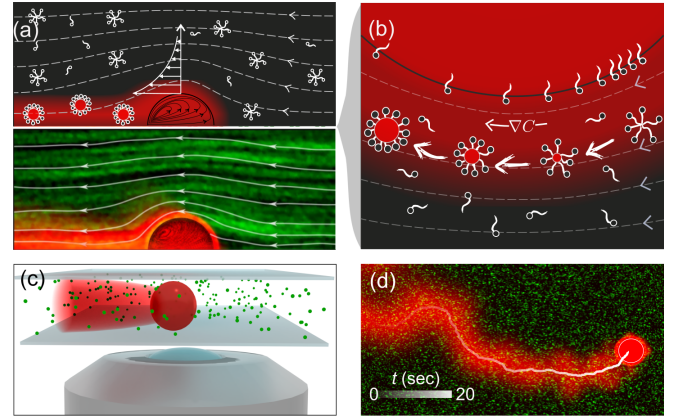


FIG. 1. Droplet propulsion mechanism and visualization technique. (a) Top: schematic illustration of the micellar solubilization of oil at the droplet interface leading to self-propulsion. Bottom: streaks of tracers following the flow inside and outside of the droplet during 2 s, with streamlines of the external flow from PIV analysis (droplet reference frame). Data are from double-channel fluorescence microscopy, with illumination at 561 (Nile Red doped oil, red emission) and 488 nm (tracer colloids, green emission). (b) Sketch of the filling and growth of micelles traveling in a boundary layer along the interface, causing a propulsive Marangoni flow. (c) Microscopy setup schematic with the droplet (radius 30 $\mu$m) swimming in a Hele-Shaw cell (height 60 $\mu$m). (d) Sample micrograph, with the droplet's centroid trajectory traced in white.

ratio of filled to empty micelles. Following an advective perturbation in the vicinity of the droplet, the initially radially isotropic cloud of filled micelles is distorted; the resulting fore-aft asymmetry generates a surface tension gradient toward the trailing oil-filled micelles which drives the droplet forward. Because of this self-sustaining gradient, the droplet propels continuously while leaving behind a trail of swollen micelles [Fig. 1(d)].

As proposed by hydrodynamic theory models [23–27], such spontaneous self-propulsion stemming from an advection-diffusion-driven interfacial instability arises only if the Péclet number Pe, which characterizes the ratio of advective to diffusive transport, exceeds a critical threshold. In a simplified description, the surfactant dynamics are approximated by treating the droplet interface as a sink for surfactant monomers [23–25]. In this framework, on which we base our subsequent mode stability analysis, Pe can be shown to be a monotonically increasing function of the swimming medium (*outer*) viscosity $\mu^o$, here nondimensionalized as $\mu = \mu^o/\mu^i$ using the constant *inner* viscosity $\mu^i$ [see Appendix B 2 for a step-by-step derivation of Eq. (1)]:

$$\text{Pe} = \frac{V_t R_d}{D} \approx \frac{18\pi^2}{k_B T} q_s r_s^2 \zeta R_d^2 \mu^i \left[ \mu \left( \frac{2\mu + 3\zeta/R_d}{2\mu + 3} \right) \right], \quad (1)$$

where $V_t$ is the theoretical terminal droplet velocity in a surfactant gradient [25,28], $R_d = 30$ $\mu$m the droplet radius,

$D = (k_B T / 6\pi r_s \mu^o)$ the diffusion coefficient for the surfactant monomer (length scale $r_s \sim 10^{-10}$ m), $q_s$ the isotropic interfacial surfactant consumption rate per area, and $\zeta \sim 10$ nm the characteristic length scale over which the surfactants interact with the droplet [24,28]. Increasing $\mu^o$ corresponds to an increase in Pe, besides the increase in viscous stresses. Henceforth, we represent an increase in $\mu^o$ by this corresponding increase in Pe, as tabulated by the color map in Fig. 2. We note that, in view of the necessary simplifications in the derivation of Eq. (1), all experimental Pe values should be regarded as approximate.

In experiments, we control $\mu^o$ via water-glycerol mixtures as the swimming medium (viscosity values in Appendix A, Fig. 7), varying the glycerol content from 0 to 70 vol % and adding the surfactant tetradecyltrimethylammonium bromide (TTAB) at 5 wt % to generate activity. Monodisperse CB15 oil droplets of radius $R_d = 30$ $\mu$m are studied in quasi-2D reservoirs 60 $\mu$m in depth for 5–6 min, a time over which the droplet radius

should not shrink by more than approximately 7%. Therefore, we do not consider any droplet size effects on Pe (see also the experimental materials and methods section in Appendix A).

## III. SIMULTANEOUS VISUALIZATION OF CHEMICAL AND HYDRODYNAMIC FIELDS

To visualize the chemical and hydrodynamic fields involved in the droplet activity, we directly image the chemical field of swollen micelles by adding the hydrophobic dye Nile Red to the oil phase [Figs. 1(c) and 1(d); see also Appendix A 5 and Supplemental Video S1 in [29] ]. The dye comigrates with the oil molecules into the filled micelles, which fluoresce when illuminated. We seed the surrounding medium, a supramicellar aqueous surfactant solution, with green fluorescent tracer colloids and measure the flow field using particle image velocimetry (PIV). The emission spectra of dye and colloids are
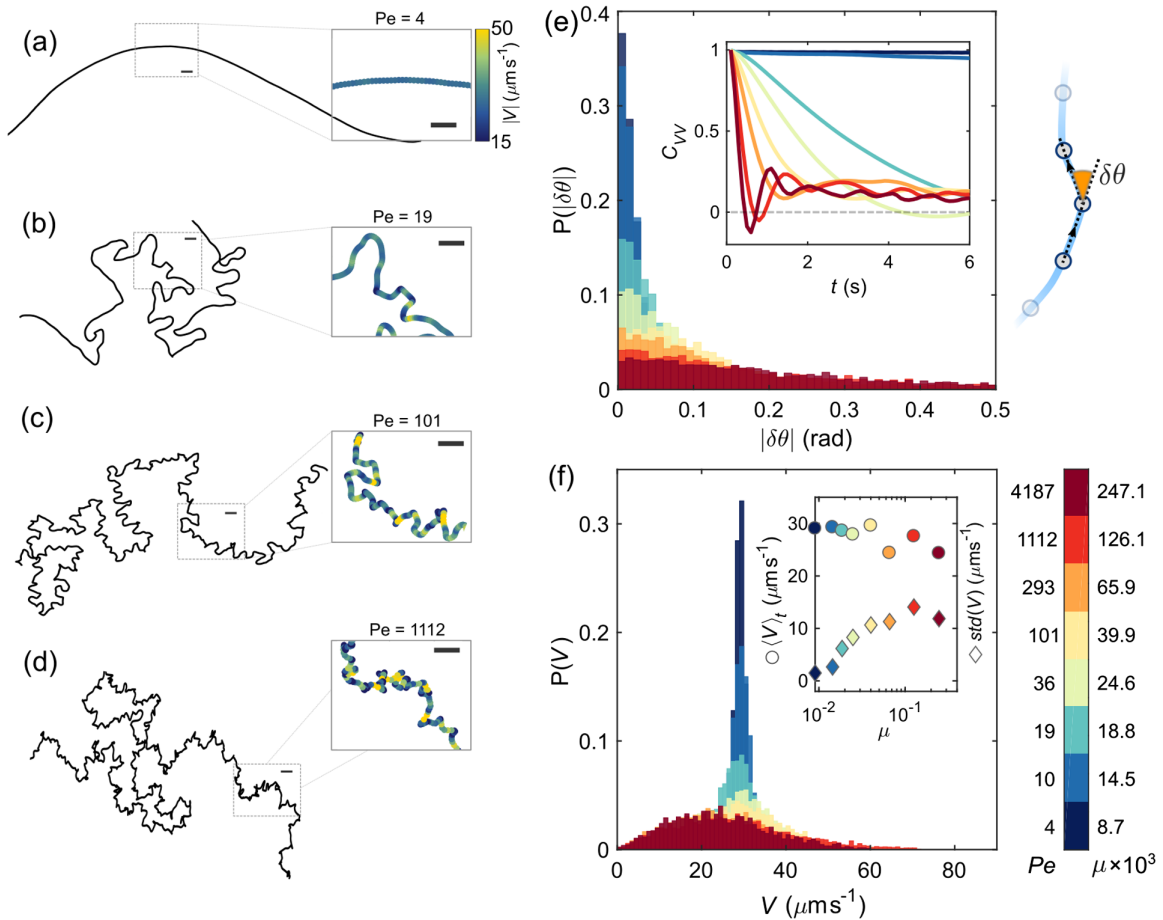


FIG. 2. Destabilized droplet motion with increasing Péclet number Pe. (a)–(d) Example trajectories of droplets for Pe $\in \{4, 19, 101, 1112\}$, with enlarged insets color coded by propulsion speed $V$. All scale bars are 50 $\mu$m. (e) Distribution of the velocity reorientation angle $|\delta\theta|$ for increasing Pe, measured during a time step $\delta t = 0.1$ s set by the video recording rate of 10 Hz. Profiles of the velocity autocorrelation function $C_{VV}$, in the inset, show the loss of directionality in swimming. (f) Distribution of propulsion speeds $V$ for increasing Pe, with mean and standard deviation of speeds in the inset. See also Supplemental Videos S2–S5 in [29]. The color bar relating experimental Pe estimates to the viscosity ratio $\mu = \mu^o/\mu^i$ applies to all subsequent figures.

sufficiently nonoverlapping to be separately detected in dual-channel fluorescence microscopy. Consequently, both fields can be simultaneously observed and analyzed; we provide an example micrograph with an overlay of the extracted droplet trajectory in Fig. 1(d). Because of the large size (approximately 5 nm) of the filled micelles, the timescale of their diffusive relaxation exceeds that of the droplet motion; thus, there is a persistent fluorescent trail in the wake of the droplet.

## IV. DESTABILIZED MOTION WITH INCREASING PÉCLET NUMBER

We begin, however, with an overview of the droplet dynamics using trajectory plots and statistical analyses of speed and orientational persistence taken from bright-field microscopy (Fig. 2). With increasing Pe, the droplet propulsion changes from uniform speeds and persistent motion to unsteady motion with abrupt reorientations [Figs. 2(a)–2(d)]. We define $P(|\delta\theta(t)|)$ as the distribution of the reorientation angle $\delta\theta$ of the 2D droplet velocity $\mathbf{V}(t)$ during a fixed time step $\delta t$ [30]:

$$\delta\theta(t) = \arctan\left(\frac{\mathbf{V}(t) \times \mathbf{V}(t + \delta t)}{\mathbf{V}(t) \cdot \mathbf{V}(t + \delta t)}\right). \qquad (2)$$

$P(|\delta\theta(t)|)$ broadens significantly, corresponding to more frequent and sharper reorientation events [Fig. 2(e)]. The faster decay of the angular velocity autocorrelation function,

$$C_{VV}(t) = \left\langle \frac{\mathbf{V}(t_0 + t) \cdot \mathbf{V}(t_0)}{|\mathbf{V}(t_0 + t)||\mathbf{V}(t_0)|} \right\rangle_{t_0}, \qquad (3)$$

illustrates the loss of directionality with increasing Pe [Fig. 2(e), inset]. Figure 2(f) shows that, at sufficiently large Pe, the speed distribution $P(V)$ includes values as small as zero (stopping events) and, surprisingly, as large as 70 $\mu$m/s, much greater than the uniform speed of 30 $\mu$m/s observed for low Pe $\approx 4$. While the mean speed barely changes with Pe, the standard deviation of $V$ grows by over one order of magnitude [Fig. 2(f), inset]. Hence, both the rotational and the translational motion of the swimmer are destabilized with increasing Pe, similar to recent numerical studies of solid phoretic particles [31]. Note that the thermal fluctuations $[O(k_b T/2R_d) \sim 10^{-16}$ N] are negligible compared to the hydrodynamic drag force $[O(6\pi\mu^o R_d V) \gtrsim 10^{-10}$ N], such that thermal noise is an unlikely cause for the unsteady swimming.

## V. SIGNATURES OF UNSTEADY DYNAMICS IN THE TIME EVOLUTION OF CHEMICAL AND HYDRODYNAMIC FIELDS

To investigate the origin of this unsteady behavior, we study the evolution of chemical and hydrodynamic fields around the droplet. We extract the tangential flow velocity

$u_\theta(\theta)$ and the red fluorescence intensity $I(\theta)$ of the chemical field close to the interface [Fig. 3(d) and Appendix A 6] and map them in kymographs $I(\theta, t)$ and $u_\theta(\theta, t)$, respectively.

For low Pe $\approx 4$, at persistent propulsion, $I(\theta, t)$ shows a single fixed-orientation band marking the origin of the filled micelle trail at the rear stagnation point of the droplet [Fig. 3(a) and Supplemental Video S6 in [29]]. The two bands in $u_\theta(\theta, t)$ correspond to a steady flow field with dipolar symmetry that is consistent with the $I(\theta, t)$ profile. On the right side of Fig. 3(a), we superimpose the streamlines of this dipolar flow field on the corresponding chemical micrograph at the time marked by I in the $I(\theta, t)$ kymograph.

For intermediate Pe $\approx 36$ [Fig. 3(b) and Supplemental Video S7 in [29]], $I(\theta, t)$ shows secondary branches forming at the anterior stagnation point of the droplet and subsequently merging with the main filled micelle trail. This observation coincides with a transient second hydrodynamic mode with quadrupolar symmetry [Fig. 3(b), II], causing the accumulation of an additional aggregate of filled micelles at the droplet anterior (see also Appendix C, Fig. 11 for additional flow field examples).

The ratio of the diffusive $(R_d^2/D_{fm})$ to advective $(R_d/V)$ timescales for the migration of filled micelles is $(VR_d/D_{fm}) \gg 1$ for all experiments, assuming a diffusion coefficient $D_{fm} = k_B T/6\pi\mu^o r_{fm}$, with a micellar radius of $O(r_{fm}) \sim 2.5$ nm. Therefore, the aggregate is unlikely to dissipate by diffusion and will continue to grow as long as the quadrupolar mode exists. However, this mode is not stable. Eventually, the dipolar mode dominates and advects the secondary aggregate toward the main trail [Fig. 3(b), III]. The transport of the aggregate along one side of the droplet locally disturbs the interfacial flow, leading to an abrupt reorientation of the swimming direction [Fig. 3(a), I–III]. As shown in the trajectories in Figs. 2(b) and 2(c), these reorientation events become more frequent with increasing Pe; accordingly, $u_\theta$ in Fig. 3(b) exhibits quasiperiodic reorientation patterns.

For high Pe $\approx 293$ [Fig. 3(c) and Supplemental Video S8 in [29]], the quadrupolar mode eventually prevails, resulting in a predominantly symmetric extensile flow around the droplet [Fig. 3(c), I], as shown by a pronounced fourfold pattern in the additional kymograph $u_r(\theta, t)$ of the radial velocity. Because of the nonpropelling quadrupolar mode, the droplet is trapped in place. The gradual accumulation of filled micelles at the two stagnation points with radially outward flow manifests in two stable branches in the chemical kymograph [marked by I in Fig. 3(c)]. The growth of the two micellar aggregates locally generates a lateral chemical gradient, which eventually pushes the droplet out of its self-made trap. Concomitantly, the two points of filled micelle emission move along the droplet interface and merge on the new rear side of the droplet into a single filled micelle trail [Fig. 3(c), II and III]. The
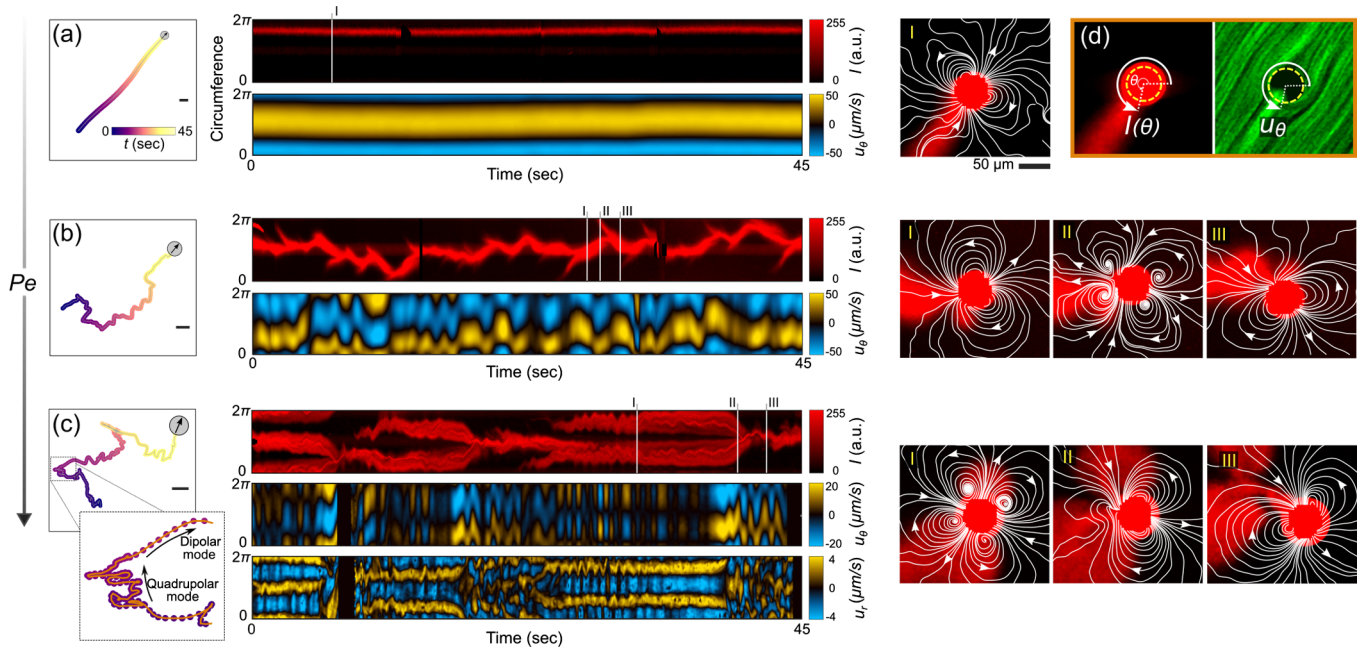
FIG. 3.   Signatures of unsteady dynamics in the time evolution of chemical and hydrodynamic fields. Rows (a), (b), and (c) correspond to $Pe \approx 4$, $Pe \approx 36$, and $Pe \approx 293$, respectively. Left column, trajectories color coded by time; middle column, kymographs of $I$ and $u_\theta$ during 45 s of propulsion; right column, selected red channel images, overlaid by the flow streamlines in the laboratory reference frame. Each frame corresponds to the point in time indicated on the kymographs by I, II, or III. (d) defines the mapping of the profiles of red light intensity $I$ (filled micelle concentration) and tangential velocity $u_\theta$ around the droplet circumference onto the $y$ axis of the kymographs in the middle column. All $u_\theta$ profiles are in the translational droplet reference frame but with $\theta = 0$ fixed at the laboratory $x$ direction to visualize the reorientation dynamics. In (c), the third kymograph corresponds to the radial velocity $u_r$ in the laboratory reference frame to better depict the quadrupolar symmetry of the flow field. The second hydrodynamic mode starts to appear at intermediate Pe and dominates the dynamics for high Pe. See also Appendix C, Fig. 11 for additional flow field examples. All scale bars are 50 $\mu$m.

chemorepulsion from the local field micelle gradient induces an apparent dipolar mode which gradually decays as the droplet leaves the self-made trap. Now, the quadrupolar mode resaturates, with an aggregate growing at the droplet anterior, until the droplet is trapped again and a new bimodal "stop-and-go" cycle begins. Since the escape direction is always lateral, consecutive runs are approximately perpendicular, resulting in the sharp reorientation events apparent in the trajectories in Figs. 3(c) and 2(d), as well as the broadening $|\delta\theta|$ distribution in Fig. 2(e).

## VI. DEPENDENCE OF HYDRODYNAMIC MODES ON THE PÉCLET NUMBER

In order to understand the dependence of the onset of bimodal motility on Pe, we analyze the underlying advection-diffusion problem for the active droplet within the framework of an axisymmetric Stokes flow as established in Refs. [23,25,26,32] (see Fig. 4 and Appendix B). At the smallest value of $\mu$, Pe is approximately equal to the critical value of 4 necessary for the onset of the first hydrodynamic mode ($n = 1$), i.e., the mode with dipolar flow symmetry [23,25,26]. With increasing $\mu$, Pe [markers in Fig. 4(a)] eventually exceeds the critical values necessary for

the onset of the higher hydrodynamic modes [lines in Fig. 4(a)], specifically the second hydrodynamic mode ($n = 2$), i.e., the mode with quadrupolar symmetry. A linear stability analysis around an isotropic, quiescent base state (see Appendix B 3 and Refs. [23,26]), which is the idealized starting point for each experiment, shows that, for small to moderate Pe, the nondimensionalized instability growth rate $\lambda$ for $n = 1$ exceeds that for $n = 2$ [Fig. 4(c)]. Accordingly, for lower Pe, $n = 1$ dominates, resulting in steady self-propulsion stemming from the fore-aft asymmetry of the surfactant distribution [Fig. 4(b), I]. Consequently, the active droplet exhibits persistent steady translation [trajectories in Figs. 2(a) and 2(b)] with a dominant dipolar flow field [Fig. 4(b), II, and Fig. 3(a)]. However, for $Pe \gtrsim 92$, $n = 2$ [Fig. 4(a), III] has a faster instability growth rate [Fig. 4(c)], thereby becoming the dominant mode when evolving from the quiescent base state. Accordingly, the droplet is initially stuck in a non-propelling mode with a quadrupolar flow field [similar to Fig. 4(b), IV]. Such a quadrupolar flow field gives rise to the filled micelle field with the two points of outflux. The synergy between the $n = 2$ mode and the transiently growing filled micelle field subsequently results in the onset of the bimodal stop-and-go motion of the droplet for
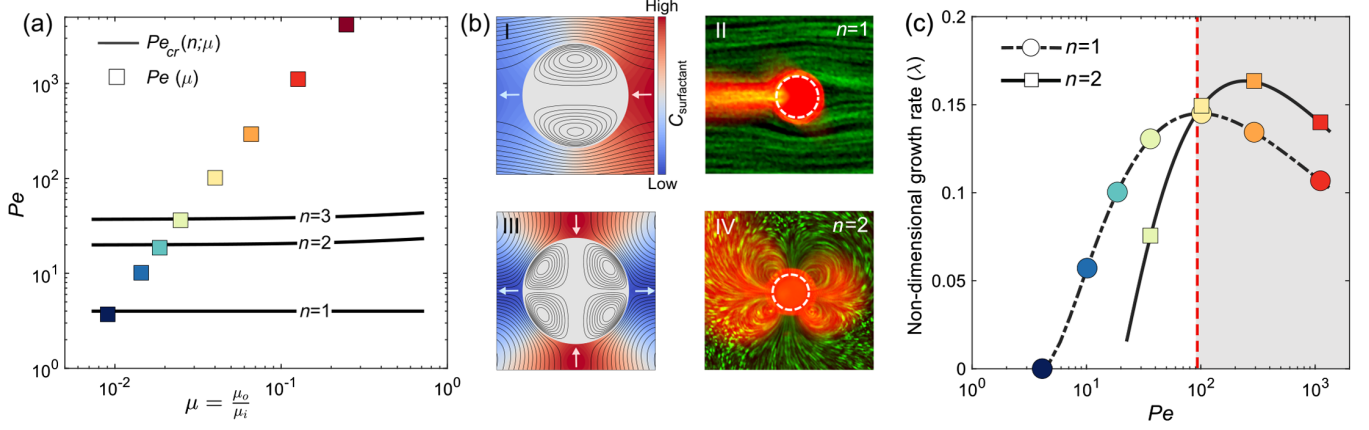
FIG. 4.    Dependence of hydrodynamic modes on the Péclet number. (a) Critical Péclet $Pe_{cr}$ values (black lines), necessary for the onset of different hydrodynamic modes ($n$), with varying $\mu$. The markers ($\square$) show the Péclet number Pe [Eq. (1)] which increases with $\mu$. The color code is taken from Fig. 2(f). (b) Top: steady self-propulsion of the active droplet; theoretical solution for $n = 1$ mode (left) and experimental streak image for low Pe (right). Bottom: the extensile flow corresponding to $n = 2$ mode (left) and the experimental image for higher Pe (right). The theoretical and the experimental flow fields are in the swimmer reference frame. (c) Instability growth rates corresponding to the first two hydrodynamic modes as a function of Pe. Beyond the dashed vertical line (gray region), $\lambda_{n=2} > \lambda_{n=1}$, and, thus, the $n = 2$ mode is dominant.

moderate to higher Pe [trajectories in Figs. 2(c) and 2(d)]. Since we observe in experiments with Pe $\gtrsim$ 100 that the active droplet experiences sustained periods of dynamical arrest during which it remains stationary with a surrounding extensile flow [Fig. 3(c)], it appears that the $n = 2$ mode can also evolve from a nonquiescent state and prevail in a similar Péclet regime as derived from the performed stability analysis. Note that we restrict our analysis to the first two hydrodynamic modes, since these two are solely responsible for the droplet propulsion and the associated far-field hydrodynamic disturbance.

## VII. INTERACTIONS WITH SELF-GENERATED CHEMICAL GRADIENTS CAUSE SPEED BURSTS

It remains to explain the broadening of $P(V)$ with increasing Pe [Fig. 2(e)], particularly the remarkable bursts in speed for high Pe. While the dipolar mode is propulsive, the quadrupolar mode is not. Hence, the growth and decay of the respective modes affect the droplet speed. As shown in Fig. 3, recurrent transitions between the two hydrodynamic modes lead to abrupt reorientation events; we therefore investigate the correlation between changes in speed and reorientation angle $|\delta\theta|$.

In a typical trajectory for intermediate Pe $\approx$ 36, each sharp turn is preceded by a deceleration and followed by an acceleration, as shown in the plot of the positional data color coded by speed in Fig. 5(c). Signatures of these correlations in the droplet dynamics appear in the conditional averages

$$\langle X(t - t_i)\rangle_i \quad \text{if } |\delta\theta(t_i)| > 0.2; \qquad \frac{d[\delta\theta(t_i)]}{dt} = 0 \quad (4)$$

of $|\delta\theta|$, $V$, and tangential acceleration $a_t$ as quantities $X$ for all sharp reorientation events $i$ in the trajectory, centered

at $t = t_i$ of maximum $|\delta\theta|$ [Fig. 5(a)]; the events are identified by choosing a threshold value of $|\delta\theta| > 0.2$ (see Appendix C, Fig. 12).

We can now directly compare these dynamics to the higher-resolution fluorescence data taken at Pe $\approx$ 36 presented in the kymographs in Fig. 3(b). Figure 5(b) shows a series of micrographs of the chemical field, with arrows marking the droplet velocity vector (black) and the position of the secondary filled micelle aggregate (white). The aggregate accumulates, is then entrained, and finally merges with the posterior trail, corresponding to the creation and merging of a secondary chemical branch in the kymograph.

For $t < 0$, the droplet decelerates while the secondary aggregate is accumulating. $t = 0$ marks the point in time where $V$ is minimal and the aggregate is on the cusp of leaving the anterior stagnation point. For $t > 0$, the aggregate is advected to the droplet posterior, and the droplet accelerates due to the resaturation of the dipolar mode. $V$ peaks once the aggregate has merged with the main trail—creating an amplified fore-aft gradient—at $t \approx 1$ s, which is comparable to the advective timescale $R_d/V \approx 1$ s. In the wide-field data analysis in Fig. 5(a), this is the time $\tau_1$ it takes the droplet to reach maximum speed after a reorientation.

We now use the correlation function between $V$ and $|\delta\theta|$, $C_{|\delta\theta|,V}(\Delta t) = \langle|\delta\theta(t)| \cdot V(t + \Delta t)\rangle_t$, plotted in Fig. 5(d), to estimate the growth times of the second mode from our data for Pe $>$ 10. Since $V$ is minimal at maximum $|\delta\theta(t)|$ [Fig. 5(d)], $C_{|\delta\theta|,V}(\Delta t)$ dips at $\Delta t = 0$. It subsequently peaks at the point of maximum $V$ with a time delay $\Delta t = \tau_1$, when the contribution of the propulsive dipolar flow is maximal. The next dip at a time $\tau_2 > \tau_1$ marks the next reorientation event; based on the discussion pertaining to Figs. 3 and 4(c), for moderate to high Pe, $\tau_2 - \tau_1$
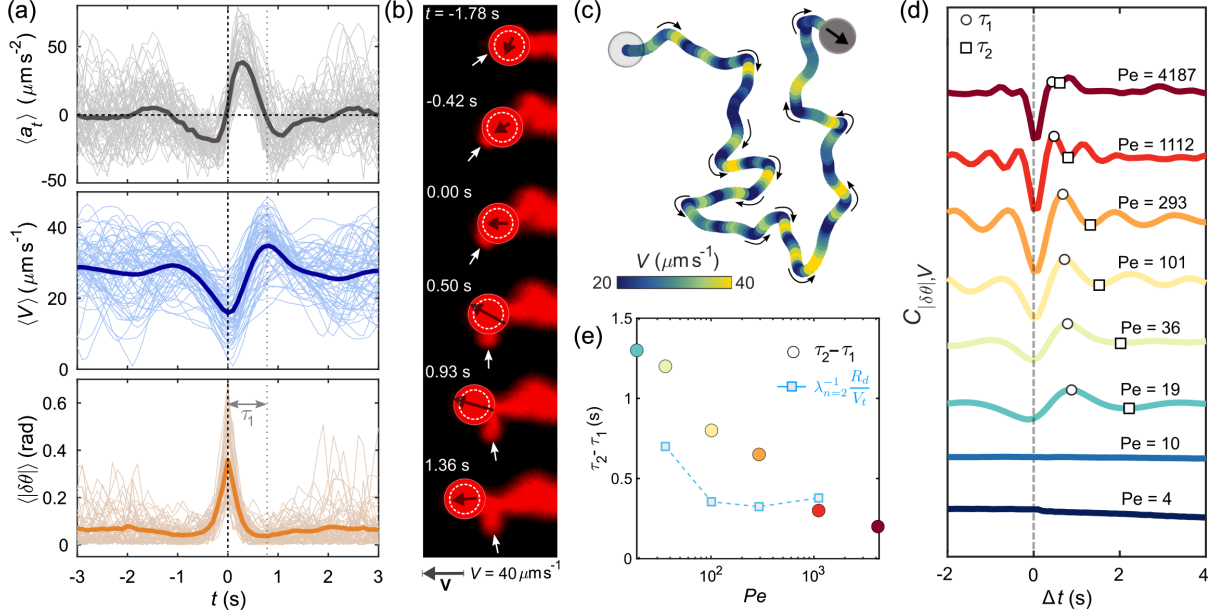
FIG. 5. Interactions with self-generated chemical gradients cause speed bursts at reorientation events. (a) Conditional averaging of tangential acceleration $a_t$, speed $V$, and reorientation angle $|\delta\theta|$, for abrupt reorientation events at Pe $\approx 36$ (see Appendix C, Fig. 12, for an illustration of the identification criteria). The dotted line marks the maximum speed at $t = \tau_1$ after reorientation. (b) Video stills of the chemical field for one such event with $t = 0$ s set to the point of minimum speed; white arrows track the accumulation of the secondary filled micelle aggregate at the anterior stagnation point and its advection along the interface, and black arrows correspond to the droplet velocity vector. The droplet speed is maximal when the secondary aggregate and the trail merge at $t = 0.93$ s. See also Supplemental Videos S9 and S10 in [29]. (c) An example trajectory for Pe $\approx 36$. Any reorientation event (curved arrows) is preceded by a deceleration and followed by an acceleration. The lowest speed occurs at the point with the highest curvature. (d) Correlation function between reorientation angle and speed, $C_{|\delta\theta|,V}(\Delta t)$ for increasing Pe. Times $\tau_1$ and $\tau_2$ (next reorientation event) are identified by the respective peak and dip in $C_{|\delta\theta|,V}$. (e) Timescale for the growth of the $n = 2$ mode versus corresponding Pe: experimentally obtained, $\tau_2 - \tau_1$ ($\circ$), compared to values from stability analysis, $\lambda_{n=2}^{-1} R_d/V_t$ ($\square$).

approximately corresponds to the timescale for the growth and resaturation of the $n = 2$ mode during the bimodal motility (i.e., starting from a nonquiescent base state). Nevertheless, we compare this experimentally obtained $\tau_2 - \tau_1$ with the theoretical growth times for the $n = 2$ mode starting from the isotropic base state, $\lambda_{n=2}^{-1} R_d/V_t$ [Fig. 4(c)], for different values of Pe. Figure 5(e) shows that these two timescales, which are strictly speaking different, still are of the same order of magnitude and show a similar decreasing trend with increasing Pe. We note that the growth time of the dipolar flow above Pe $\approx 100$ cannot be used for comparison to $\lambda_{n=1}$, since this flow is imposed by the lateral chemical gradient. However, we can assume that this gradient increases with Pe, resulting in faster acceleration, markedly higher swimming speeds, and, hence, reduced $\tau_1$, as observed experimentally [Fig. 5(d)].

## VIII. CONSEQUENCES FOR SPATIAL EXPLORATION

Reminiscent of gait-switching dynamics in biological locomotion, we demonstrate the emergence of complex swimming behavior in a minimal active droplet system by tuning the Péclet number. We find a transition from persistent swimming at low Pe to chaotic bimodal swimming at high Pe—the latter results from the excitation of higher hydrodynamic modes beyond critical Pe values, while the continuous switching between them is caused by the self-generated chemical gradient in the environment.

This gradient sensitivity causes trail avoidance [16], which, in turn, affects the way these droplet swimmers explore their environment. With increasing reorientation frequency, we find a transition from quasiballistic propulsion to a 2D self-avoiding walk (2D SAW). This effect is illustrated by the trajectories in Figs. 2(a)–2(d) and also by the fact that $C_{VV}$ in Fig. 2(e) does not decay to zero. For a statistical analysis, we plot mean squared displacements for selected Pe values in Fig. 6(a), which reproduce the expected scaling with $t^2$ (ballistic) for Pe $\approx 4$ and a transition to $t^{3/2}$ (2D SAW [33]) for Pe $\gtrsim 36$, with the crossover time decreasing with increasing Pe. While transitions to random walks governed by run-and-tumble gait switching are common in bioswimmers [34], self-avoidance requires chemical self-interaction [35].

Examples of anomalous diffusion driven by repulsive biochemical signaling are found in the spreading of slime
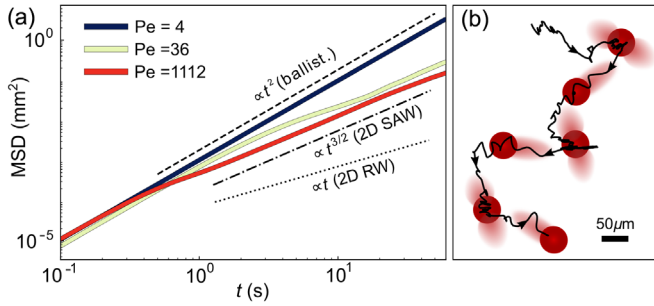
FIG. 6. Anomalous diffusive swimming. (a) Mean squared displacement profiles of experimental trajectories for different Pe. Dashed lines mark the predicted scaling for ballistic motion, $\propto t^2$, 2D self-avoiding walk (SAW), $\propto t^{3/2}$, and random walk (RW), $\propto t$. For higher Pe, there is a transition from ballistic to 2D SAW. (b) A segment of the trajectory associated with the SAW and schematics of the droplet exhibiting bimodal swimming causing the SAW. See also Appendix C, Fig. 13.

molds [36,37]—active droplets can show analogous behavior based on purely physicochemical mechanisms.

## IX. CONCLUSION

In this work, we demonstrate that the manner in which hydrodynamic and self-generated chemical fields are coupled determines the nonlinear dynamics of autophoretic microswimmers. The fluorescence-based visualization technique used to simultaneously probe this coupling can provide insight into many recent autophoretic models [20,21,23,24,38–40]. For example, extensive theoretical studies [41–44] demonstrate the importance of quantifying far-field and near-field contributions, coupling to chemical fields, and the effects of confinement to understand how swimmers approach each other or form bound states, which is vital to nutrient entrainment, food uptake, and mating in bioswimmers.

While many microswimmer models incorporate unsteady dynamics via stochastic fluctuations, we show that the interplay of nonlinear dynamics and interaction with the history of motion also allows for the emergence of memory-driven chaotic behavior. An appealing example from a different field are droplet walkers on a vibrated bath [45], which show a transition from persistent to a bimodal, stop-and-go motion based on an effective "system memory" parameter [46,47]. The corresponding theoretical framework [46] is general enough to also apply to bimodal chaotic motion in droplet swimmers.

## ACKNOWLEDGMENTS

## APPENDIX A: MATERIALS AND METHODOLOGY

### 1. Materials and characterization

Our samples consist of droplets of (S)-4-cyano-4'-(2-methylbutyl)biphenyl (CB15) doped with the fluorescent dye Nile Red in an aqueous solution of the cationic surfactant TTAB corresponding to 5 wt % (50 mg in 1 ml of solution) in pure water, with a critical micelle concentration of CMC = 0.13 wt %. We purchase CB15, TTAB, and Nile Red from commercial suppliers (Synthon Chemicals and Sigma-Aldrich) and use them as is. We control the viscosity of the swimming medium $\mu_o$ by adding glycerol to the aqueous TTAB solution.

We use an Anton Paar MCR 502 rotational rheometer to characterize the shear viscosity of water-glycerol-surfactant solutions (Fig. 7). Experiments are carried out using a cone-plate geometry, to find shear-rate versus shear-stress curves at a fixed temperature and viscosity versus temperature at a fixed shear rate. To limit effects of solution evaporation, the cone-plate geometry is surrounded by a water bath and covered by a Peltier hood. Over the shear rate range $0.01 \text{ s}^{-1} < \dot{\gamma} < 100 \text{ s}^{-1}$, viscosity is found to be constant, such that our solutions are well described as Newtonian, as should be expected: Water-glycerol mixtures are used as Newtonian standard media throughout the existing literature.

To estimate the surfactant consumption rate $q_s$ in Eq. (1), we extract the droplet shrinking rate $dR_d/dt$ from the bright-field microvideography data presented in Fig. 2. We find a moderate dependence on the glycerol fraction (Fig. 8), which we include as a first-order approximation, via linear regression (blue line), to evaluate $q_s$ in the Pe estimates in the main manuscript.
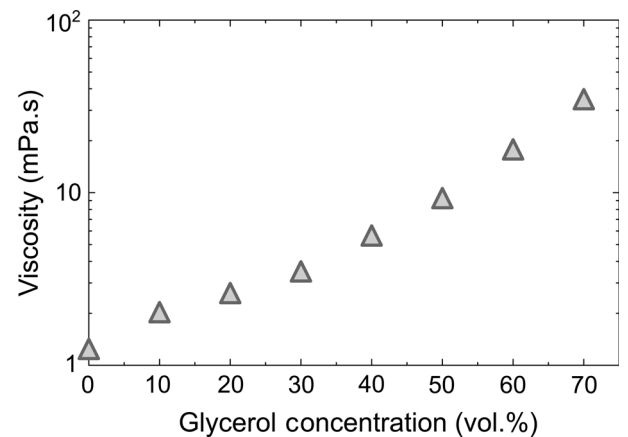


FIG. 7. Viscosity of the swimming medium, a mixture of water, glycerol, and TTAB surfactant, for increasing glycerol-water ratios. Surfactant concentration is 50 mg in 1 ml of solution.
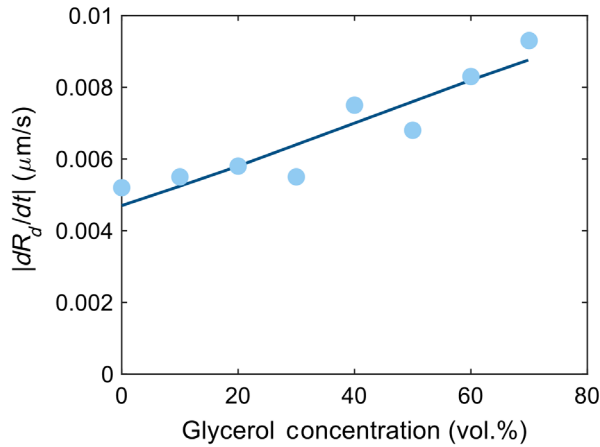
FIG. 8. Solubilization rate $|dR_d/dt|$, for increasing glycerol-water ratios; the blue line marks a linear regression fit to $y = 0.000058x + 0.0047$. Surfactant concentration is 50 mg in 1 ml of solution.

## 2. PDMS soft lithography for droplet generation

For the production of monodisperse oil droplets, we fabricate microfluidic channels in house, using standard soft lithography techniques. First, 2D photomasks are designed in AutoCad and then printed onto an emulsion film in high-resolution (128 000 dpi) by a commercial supplier (JD Photo-Tools). Next, the photoresist SU-8 3025 (MicroChem) is spin coated onto a 4-inch-diameter silicon wafer (Si-Mat), where spin speed and duration are adjusted to give a controllable uniform thickness. A negative mold is cured in the SU-8 through the photomask by UV light exposure. After further chemical treatment with photoresist developer, uncured SU-8 is removed, leaving behind cured SU-8 microstructures on the silicon wafer.

We then pour a poly(dimethyl siloxane) (PDMS, Sylgard 184, Dow Corning) mixture of 10∶1 volumetric ratio of base to cross-linker over the wafer and bake for 2 h at 80 °C, producing a solid PDMS layer with microstructured indentations. We peel the indented PDMS from the wafer and punch holes through it to create liquid inlets and outlets at opposing ends of the channels. The structured PDMS surface, as well as a glass cover slip, are cleaned and treated with partial pressure air plasma (Pico P100-8; Diener Electronic GmbH+Co. KG) for 30 s and then pressed together, bonding the two surfaces. Figure 9 shows a micrograph of such a PDMS chip during droplet production.

The walls of these microfluidic chips are selectively treated to hydrophilize the channels where surfactant solution will flow. This treatment prevents oil from wetting the walls during droplet production. We follow the technique of Petit *et al.* [48]: First, the channel walls are oxidized by a 1∶1 mixture of hydrogen peroxide solution (H2O2 at 30 wt %, Sigma-Aldrich) and hydrochloric acid (HCl at 37 wt %, Sigma-Aldrich). This mixture is flushed through the channels for approximately 2 min by using a vacuum pump
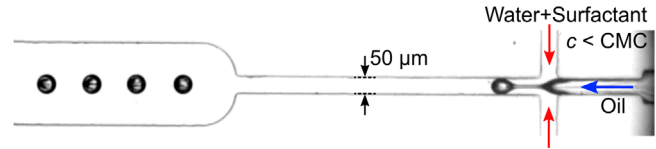


FIG. 9. The microfluidic chip used to produce monodisperse oil droplets in a surfactant solution.

system. After the oxidation, the channel is rinsed by flushing double distilled water for 30 s. Next, a 5 wt % solution of the positive polyelectrolyte poly(diallyldimethylammonium chloride) (PDADMAC, Sigma-Aldrich) is flushed for 2 min through the oxidized channel of the device. The PDADMAC binds to the activated channel walls by ionic interactions. Finally, a 2 wt % solution of the negative polyelectrolyte poly(sodium 4-styrenesulfonate) (PSS, Sigma-Aldrich) is flushed for 2 min.

## 3. Droplet generation

Once the chips are treated, we mount syringes of oil and 0.1 wt % aqueous TTAB solution to a microprecision syringe pump (NEM-B101-02B; Cetoni GmbH), connect these to the two inlets of the microfluidic chip via Teflon tubing (39241; Novodirect GmbH), and tune the flow speed through the chip until the desired droplet size is reached. Once droplet production is monodisperse (after approximately 5 min) and at a steady state, these droplets are collected in a bath of 0.1 wt % TTAB solution. This solution is of a high enough concentration to stabilize the droplets against coalescence but not high enough to induce solubilization.

## 4. Fabrication of the observation Hele-Shaw cell

The swimming behavior of the droplets is observed in a quasi-2D Hele-Shaw reservoir, which we fabricate directly from SU-8 photoresist without PDMS casting. To fabricate the reservoirs, we therefore use a photomask with inverted polarity. We spin coat the photoresist directly onto a glass slide ($50 \times 75$ mm$^2$) and follow the same procedure for photolithography as outlined in Appendix A 2. This process results in a layer of cross-linked SU-8 (thickness approximately 60 $\mu$m) with reservoirs of the dimensions $8 \times 13$ mm. These reservoirs are filled with the samples, sealed with a glass cover slip, and put under a microscope.

## 5. Double-channel fluorescent microscopy technique

We use double-channel fluorescent microscopy for simultaneous imaging of the chemical and hydrodynamic fields. A schematic of the setup is shown in Fig. 10. Two laser units excite the test section. The Nile Red dye (Thermo Fisher Scientific), which visualizes the oil phase, is excited with a 561 nm laser and emits light at a maximum of approximately 630 nm. The green fluorescent particles (FluoSpheres[TM], yellow-green fluorescent, 500 nm in
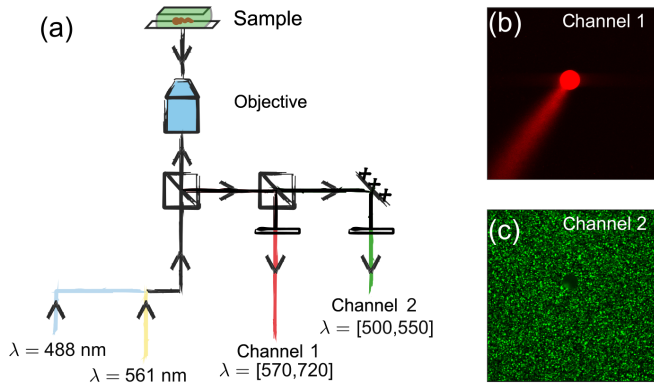
FIG. 10.   Dual-channel fluorescent microscopy. (a) Light path schematic with excitation laser lines. (b),(c) Example micrographs showing the separated emission from filled micelles (b) and fluorescent tracers (c).

diameter), which visualize the fluid flow around the droplet, are excited with a 488 nm laser and emit light at a maximum of approximately 510 nm. The emitted light is separated using a beam splitter and appropriate filters for each emission maximum. We also use a spatial pinhole (confocal microscopy) to enhance image quality. Examples of snapshots recorded on each channel are shown in Figs. 10(b) and 10(c).

### 6. Image processing and data analysis

To observe the long-time statistical behavior of the active droplets, as in Fig. 2, we observe their motion in a glass-bounded Hele-Shaw cell (quasi-two-dimensional reservoir, $13 \times 8$ mm and height $h \approx 60$ $\mu$m) under a bright-field microscope (Leica DM4000 B) at low magnification ($5\times$) compared to the double-channel fluorescence microscopy setup. Videos are recorded at a frame rate of ten frames per second using a Canon (EOS 600d) digital camera ($1920 \times 1080$ px). The droplet coordinates in each frame are extracted from video frames using the common Python libraries numpy, PIL, and openCV (scripts available on request). Steps include background correction, binarization, blob detection by contour analysis, and minimum enclosing circle fits. Swimming trajectories are obtained using a frame-by-frame nearest-neighbor analysis.

To acquire the kymographs of the chemical field and tangential and radial velocities around the droplet interface, we observe the droplet behavior by double-channel fluorescent microscopy as described in Appendix A 5. We use a $512 \times 512$ pixel camera at a frame rate of 14 frames per second connected to a $20\times$ objective. First, we split the red (Nile Red, filled micelles) and green (tracer particles) channels. Then, the red frames are used to extract the droplet coordinates via the blob detection algorithm described above. We use a MATLAB script that centers the droplet and records the red light intensity value along the interface at a distance 15.6 $\mu$m for Pe $\approx 4$ and 36 and

20.4 $\mu$m for Pe $\approx 293$. We note that it is not possible to record the intensity closer to the interface, because the strong fluorescence from the large amounts of dye inside the droplet create a very bright region extending several micrometers beyond the actual interface. We plot the extracted profiles versus time to generate spatiotemporal kymographs.

For a quantitative analysis of the flow field around the droplet, we perform particle image velocimetry (PIV) on the tracer particles images (green channel) using the MATLAB-based PIVlab interface [49]. The objective is focused on the midplane of the Hele-Shaw cell. We define a moving mask for the area covered by the droplet. We perform the analysis in $16 \times 16$ pixel interrogation windows with 75% overlap. The spatial resolution is 1.2 $\mu$m/px. After obtaining the velocity vector field, we center the droplet and read the velocity vectors at a certain distance from the droplet interface (3.6 $\mu$m for Pe $\approx 4$ and 36 and 8.4 $\mu$m for Pe $\approx 293$). The tangential ($u_\theta$, in the droplet reference frame) and radial ($u_r$, only for Pe $\approx 293$, in the lab reference frame) velocity components are then calculated and plotted in the kymographs. Because of the impermeability boundary condition, the radial component of the velocity directly at the interface is supposed to be zero; however, since we read the values at a certain distance from the interface, there is an inward and outward radial contribution to the flow. We use this observation, in particular, at Pe $\approx 293$ to show the quadrupolar symmetry of the flow field at the stopping moment.

In Fig. 1(a) and Supplemental Video S1 in [29], we track the droplet and center it in the image. To obtain the path lines of the tracer particles in the video, we use FlowTrace [50] to convolve a superposition of ten frames for each image. For Fig. 1(a), we superimpose 30 frames. To visualize the motion of the tracer particles in Fig. 4(b), IV, and the Supplemental Videos S6–S9 in [29], we process the green channel of the input video (8-bit RGB) as follows: For each pixel coordinate, the intensity is replaced by its standard deviation within a 20-frame window around the current frame. Each frame is subsequently contrast maximized within a [0, 255] intensity range. The red and blue channels are not modified. This procedure is inspired by ImageJ's Z projection algorithm; the respective Python code is available on request.

### APPENDIX B: VISCOSITY DEPENDENCE OF HYDRODYNAMIC MODES

In this appendix, we describe the mathematical framework for the coupled hydrodynamic and advection-diffusion problems pertaining to the active droplet system. Note that we follow the solution methodology of Refs. [23,25,26] and rework each step of the analysis for the present system. The appendix shows the origins of all expressions and equations (including the scaling analyses necessary for simplifications) needed to understand the

theoretical framework and, importantly, the origin of Fig. 4. We especially show each step of the linear stability analysis so that the derivation of the equations governing the instability growth rates for the hydrodynamic modes is clear.

### 1. Governing equations and boundary conditions for the active droplet system

Considering *an axisymmetric Stokes flow* (Reynolds number for the swimming of the active droplet Re $\sim 10^{-4}$) and *the impermeability of the droplet interface*, the flow field around and inside the *spherical* active droplet (capillary number Ca $\ll 1$) can be expressed in terms of the *nondimensional* stream function $\psi$, in $(r, \theta)$ coordinate system, as [25,26,32]

$$\psi^o = a_1 \left( \frac{1}{r} - r^2 \right) (1 - \eta^2) P'_1(\eta)$$
$$+ \sum_{n=2}^{\infty} a_n \left( \frac{1 - r^2}{r^n} \right) (1 - \eta^2) P'_n(\eta), \quad \text{(B1)}$$

$$\psi^i = \sum_{n=1}^{\infty} b_n (r^{n+1} - r^{n+3})(1 - \eta^2) P'_n(\eta). \quad \text{(B2)}$$

Here, and in the subsequent discussions, superscripts $o$ and $i$ refer to quantities outside and inside the active droplet, respectively, $r$ is the radial coordinate nondimensionalized by droplet radius $R_d$, $\eta = \cos\theta$, and $P_n(\eta)$ is the Legendre polynomial of degree $n$ with the prime denoting its derivative; $n$ here physically represents the $n$th hydrodynamic mode. The *nondimensional* radial and tangential flow velocity components around and inside the droplet are related to $\psi$ as $u_r = -(1/r^2)(\partial\psi/\partial\eta)$ and $u_\theta = -[1/r(1 - \eta^2)^{1/2}](\partial\psi/\partial r)$. The coefficients $a_n$ and $b_n$ in Eqs. (B1) and (B2) are constrained by the following boundary conditions [25,32].

(i) *tangential velocity* $(u_\theta)$ *condition at the droplet interface* $(r = 1)$.

$$u_\theta^o - u_\theta^i = m \left( \frac{2\mu + 3}{1 + 3m} \right) (1 - \eta^2)^{1/2} \left( \frac{\partial c}{\partial \eta} \right)_{r=1}. \quad \text{(B3)}$$

(ii) *tangential stress* $(\tau_{r\theta})$ *condition at the droplet interface* $(r = 1)$ *(Marangoni effect)*.

$$\tau_{r\theta}^o - \tau_{r\theta}^i = -\frac{1}{\mu} \left( \frac{2\mu + 3}{1 + 3m} \right) (1 - \eta^2)^{1/2} \left( \frac{\partial c}{\partial \eta} \right)_{r=1}. \quad \text{(B4)}$$

The coefficients on the right-hand side of Eqs. (B3) and (B4) essentially stem from the nondimensionalization of the classical boundary conditions. Note that the flow velocity

is nondimensionalized using $V_t = [q_s(\gamma_c R_d + 3\mu^i M)/D(2\mu^o + 3\mu^i)]$, which is a theoretical estimate for the terminal velocity of the active droplet considering the contributions of both the Marangoni and the diffusiophoretic effects [25,28]. Furthermore, $\mu = \mu^o/\mu^i$ is the ratio of the swimming medium viscosity $\mu^o$ to the droplet viscosity $\mu^i$, and the nondimensional parameter $m$ represents the relative strengths of diffusiophoretic to Marangoni effects [25]. Essentially, $m$ can be considered as a ratio of the diffusiophoretic velocity scale to the viscocapillary velocity scale representing the Marangoni effect. Accordingly, $m = (\mu^i M/\gamma_c R_d) \approx (\zeta/2R_d\mu)$, where $M \approx (k_B T/2\mu^o)\zeta^2$ is the diffusiophoretic mobility [24,28], $\gamma_c \approx k_B T\zeta$ is the leading-order change in the interfacial surface tension $\gamma$ with surfactant concentration $c$ (alternatively, $\gamma_c = (d\gamma/dc)$ can be considered to be a measure of the change in $\gamma$ with $c$ assuming a linear variation) [24,25], and $\zeta \sim 10$ nm is the characteristic length scale over which the surfactants interact with the droplet in the interfacial region. For the active droplet system, $O(m) \sim 10^{-3} - 10^{-2}$ for the entire range of experiments; hence, for the present physical problem, the diffusiophoretic effect is much weaker as compared to the Marangoni effect. However, the former is considered in the analysis here for the sake of generality. In the definition of $V_t$, $q_s$ is an isotropic and constant interfacial surfactant consumption rate per unit area necessary for the droplet activity, and $D = (k_B T/6\pi r_s\mu^o)$ is the diffusion coefficient for the surfactant monomer (length scale for surfactant monomer $r_s \sim 10^{-10}$ m). $q_s$ can be approximately estimated by assuming that the total number of surfactant monomers necessary per unit time to account for the volumetric reduction rate of the droplet due to the formation of the filled micelles is equal to the total interfacial surfactant consumption rate. Hence, $|dV_d/dt|N_s/v_{fm} \approx q_s 4\pi R_d^2$, which implies that $q_s \approx (3N_s|dR_d/dt|)/(4\pi r_{fm}^3)$. Here, $O(N_s) \sim 25$ is the number of surfactant monomers per filled micelle, $v_{fm} = 4/3\pi r_{fm}^3$ is the filled micelle volume with a micellar radius of $O(r_{fm}) \sim 2.5$ nm, and $|dR_d/dt|$ is the droplet solubilization rate as given in Fig. 8.

Equations (B3) and (B4) delineate the dependence of the swimming hydrodynamics on the distribution of the nondimensional surfactant concentration $c$ in the vicinity of the droplet. Naturally, $c$ is governed by an advection-diffusion relation [25,26,32]:

$$\text{Pe} \left[ u_r^o \frac{\partial c}{\partial r} - \frac{u_\theta^o}{r} (1 - \eta^2)^{1/2} \frac{\partial c}{\partial \eta} \right]$$
$$= \frac{1}{r^2} \frac{\partial}{\partial r} \left( r^2 \frac{\partial c}{\partial r} \right) + \frac{1}{r^2} \frac{\partial}{\partial \eta} \left( (1 - \eta^2) \frac{\partial c}{\partial \eta} \right). \quad \text{(B5)}$$

The distribution of $c$ is subject to the following boundary conditions:

(i) *isotropic and constant surfactant consumption at the droplet interface* ($r = 1$).

$$\left(\frac{\partial c}{\partial r}\right)_{r=1} = 1. \qquad (B6)$$

(ii) *the bulk condition.*

$$c(r \to \infty) \to c_\infty. \qquad (B7)$$

Note that Eq. (B6) addresses the depletion of the interfacial surfactant monomers due to the creation of the filled micelles by considering the isotropic and constant interfacial surfactant adsorption rate per unit area of $q_s$, corresponding to a flux with unit of number per area per time (in dimensional form, $D\nabla c^* \cdot \hat{n} = q_s$; this estimate gives a scale for the surfactant concentration as $\sim(q_s R_d/D)$) [25,26]. Pe in Eq. (B5) is the system Péclet number—the details of which are discussed in the following subsection. The above system of equations [Eqs. (B1)–(B7)] can be solved for $\psi$ (therefore, $u_r$ and $u_\theta$) and $c$ using the singular perturbation technique for certain limiting cases [25,26]. The solvability condition clearly shows that the actuations of different hydrodynamic modes depend on certain threshold values of Pe [Fig. 4(a) in the main text] [25]. Furthermore, the asymptotic analysis also provides a physical understanding of the hydrodynamic and surfactant concentration fields corresponding to the different modes, specifically $n = 1$ and $n = 2$ [Fig. 4(b) in the main text].

### 2. The system Péclet number

The important thing to understand now is the dependence of Pe on $\mu$. Classically, Pe can be written as Pe $= (V_t R_d/D)$, where $V_t = [q_s(\gamma_c R_d + 3\mu^i M)/D(2\mu^o + 3\mu^i)]$ is the theoretical estimate for the terminal velocity of the active droplet considering the contributions of both the Marangoni and diffusiophoretic effects, as mentioned in the preceding subsection [25,28]. Utilizing the aforementioned definition of $V_t$ and following some simple algebraic manipulations, Pe can be expressed in terms of system constants and the parameter $\mu$ as

$$\text{Pe} = \frac{V_t R_d}{D} = \frac{q_s(\gamma_c R_d + 3\mu^i M)}{D(2\mu^o + 3\mu^i)}\frac{R_d}{D}$$

$$\Rightarrow \text{Pe} = \frac{q_s M}{Dm}\frac{(1 + 3m)}{(2\mu + 3)}\frac{R_d}{D}$$

$$\Rightarrow \text{Pe} \approx \frac{18\pi^2}{k_B T}q_s r_s^2 \zeta R_d^2 \mu^i \left[\mu\left(\frac{2\mu + 3\zeta/R_d}{2\mu + 3}\right)\right]. \qquad (B8)$$

In the last step of Eq. (B8), the approximate expressions for $M$ and $m$ (see Appendix B 1) and the definition of $D$ (see Appendix B 1) are utilized to derive the final

expression for Pe. Equation (B8) expresses Pe as a monotonically increasing function of the viscosity ratio $\mu$ [markers in Fig. 4(a) in the main text]. Note that $q_s$ is approximately estimated by relating the dissolution rate of the active droplet to the isotropic and constant surfactant consumption at the droplet interface [24]; the dissolution rate of the active droplet is dependent on the glycerol concentration (Fig. 8), which effectively makes $q_s$ dependent on $\mu_o$. We further note that the second term in the numerator within parentheses $O(\zeta/R_d) \sim 10^{-4}$; this small magnitude further substantiates the fact that the diffusiophoretic effect is much weaker compared to the Marangoni effect for the present system.

### 3. Linear stability analysis about a motionless (isotropic) base state

For the linear stability analysis (also see Refs. [23,26]), the time-dependent form of the advection-diffusion equation [Eq. (B5)] is used:

$$\text{Pe}\left[\frac{\partial c}{\partial t} - \frac{1}{r^2}\frac{\partial\psi^o}{\partial\eta}\frac{\partial c}{\partial r} + \frac{1}{r^2}\frac{\partial\psi^o}{\partial r}\frac{\partial c}{\partial\eta}\right]$$
$$= \frac{1}{r^2}\frac{\partial}{\partial r}\left(r^2\frac{\partial c}{\partial r}\right) + \frac{1}{r^2}\frac{\partial}{\partial\eta}\left((1 - \eta^2)\frac{\partial c}{\partial\eta}\right). \qquad (B9)$$

Next, the desired quantities are expressed in terms of the unsteady (instability) modes—$\psi = e^{\lambda t}\sum_n \tilde{\psi}_n(r)P_n(\eta)$ and $c = -(1/r) + e^{\lambda t}\sum_n \tilde{c}_n(r)P_n(\eta)$, where $\lambda(>0)$ is the non-dimensional growth rate for the instability modes. Using the aforementioned expressions for $\psi$ and $c$ and linearizing Eq. (B9), the governing equations for the first two modes can be obtained as

$$\frac{d}{dr}\left(r^2\frac{d\tilde{c}_1}{dr}\right) - (2 + \lambda_s^2 r^2)\tilde{c}_1 = 2\text{Pe}a_1\frac{1 - r^3}{r^3}, \qquad (B10)$$

$$\frac{d}{dr}\left(r^2\frac{d\tilde{c}_2}{dr}\right) - (6 + \lambda_s^2 r^2)\tilde{c}_2 = 6\text{Pe}a_2\frac{1 - r^2}{r^4}, \qquad (B11)$$

where $\lambda_s = \sqrt{\lambda\text{Pe}}$ and $a_1$ and $a_2$ are the coefficients of the first and second modes, respectively, of the outer stream function [as in Eq. (B1)]. Equations (B10) and (B11) are solved to evaluate $\tilde{c}_1$ and $\tilde{c}_2$, respectively:

$$\tilde{c}_1 = \text{Pe}a_1\left(\frac{2}{x^2} + \frac{\lambda_s^3}{2x^3}\right) + \alpha_1\left(\frac{1 + x}{2x^2}\right)e^{-x}$$
$$- \text{Pe}a_1\frac{\lambda_s^3}{4x^2}\left[\left(\frac{1 + x}{2}\right)[Chi(x) + Shi(x)]e^{-x}\right.$$
$$\left. - \left(\frac{1 - x}{2}\right)[Chi(x) - Shi(x)]e^x\right], \qquad (B12)$$

$$\tilde{c}_2 = \text{Pe}\frac{a_2}{8}\left(\frac{8\lambda_s^4}{x^4}+\frac{\lambda_s^4}{x^2}-\frac{6\lambda_s^2}{x^2}\right)+\alpha_2\left(\frac{x^2+3x+3}{2x^3}\right)e^{-x}$$

$$+\text{Pe}a_2\frac{\lambda_s^2(6-\lambda_s^2)}{16x^3}\{(x^2+3x+3)[Chi(x)+Shi(x)]e^{-x}$$

$$-(x^2-3x+3)[Chi(x)-Shi(x)]e^x\}. \qquad (B13)$$

Here, $x = r\lambda_s$ is a rescaled spatial variable, $Chi(x)$ and $Shi(x)$ are the hyperbolic cosine integral and hyperbolic sine integral functions, respectively, and $\alpha_1$ and $\alpha_2$ are the constants of integration. Note that Eqs. (B12) and (B13) are evaluated in a manner which satisfies the bulk condition for the surfactant distribution [Eq. (B7)], i.e., as $r \to \infty$, $c - c_\infty \to 0$. Furthermore, considering the expression for $c$, the interfacial surfactant consumption condition [Eq. (B6)] reduces to the form

$$\left(\frac{\partial c}{\partial r}\right)_{r=1}=1 \Rightarrow \left(\frac{d\tilde{c}_1}{dx}\right)_{x=\lambda_s}=0; \quad \left(\frac{d\tilde{c}_2}{dx}\right)_{x=\lambda_s}=0. \quad (B14)$$

Using Eqs. (B12) and (B14), $\alpha_1$ can be evaluated as

$$\alpha_1 = -\text{Pe}a_1\frac{e^{\lambda_s}}{4(\lambda_s^2+2\lambda_s+2)}\{2(\lambda_s^4+6\lambda_s^2+16)$$

$$+\lambda_s^3(\lambda_s^2-2\lambda_s+2)[Chi(\lambda_s)-Shi(\lambda_s)]e^{\lambda_s}$$

$$-\lambda_s^3(\lambda_s^2+2\lambda_s+2)[Chi(\lambda_s)+Shi(\lambda_s)]e^{-\lambda_s}\}. \quad (B15)$$

Similarly, using Eqs. (B13) and (B14), $\alpha_2$ can be evaluated as

$$\alpha_2 = \text{Pe}a_2\frac{\lambda_s^2 e^{\lambda_s}}{8(\lambda_s^3+4\lambda_s^2+9\lambda_s+9)}\{-2\lambda_s(5\lambda_s^2+2)$$

$$+(\lambda_s^2-6)(\lambda_s^3-4\lambda_s^2+9\lambda_s-9)[Chi(\lambda_s)-Shi(\lambda_s)]e^{\lambda_s}$$

$$+(\lambda_s^2-6)(\lambda_s^3+4\lambda_s^2+9\lambda_s+9)[Chi(\lambda_s)+Shi(\lambda_s)]e^{-\lambda_s}\}. \qquad (B16)$$

Equations (B12) and (B13), along with Eqs. (B15) and (B16), give closed form expressions for $\tilde{c}_1$ and $\tilde{c}_2$.

Considering the hydrodynamic boundary conditions [Eqs. (B3) and (B4)] and using the orthogonality condition for Legendre polynomials, a set of two simple algebraic equations for the coefficients $a_n$ and $b_n$ for each of the first two modes can be written as

(i) first mode ($n = 1$):

$$3a_1 - 2b_1 = m\left(\frac{2\mu+3}{1+3m}\right)\tilde{c}_1, \qquad (B17)$$

$$\mu a_1 + b_1 = \frac{1}{6}\left(\frac{2\mu+3}{1+3m}\right)\tilde{c}_1. \qquad (B18)$$

(ii) second mode ($n = 2$):

$$a_2 - b_2 = \frac{m}{2}\left(\frac{2\mu+3}{1+3m}\right)\tilde{c}_2, \qquad (B19)$$

$$\mu a_2 + b_2 = \frac{1}{10}\left(\frac{2\mu+3}{1+3m}\right)\tilde{c}_2. \qquad (B20)$$

Note that $\tilde{c}_n$ in the above equations is explicitly dependent on $a_n$ [see Eqs. (B12) and (B15) and Eqs. (B13) and (B16)]. Considering the closed form expression for $\tilde{c}_1$ [Eqs. (B12) and (B15)], the solvability condition for Eqs. (B17) and (B18) gives

$$\frac{-[Chi(\lambda_s)-Shi(\lambda_s)]e^{\lambda_s}\lambda_s^4-\lambda_s^3+\lambda_s^2-2\lambda_s+6}{12(\lambda_s^2+2\lambda_s+2)}=\frac{1}{\text{Pe}}. \quad (B21)$$

Similarly, considering the closed form expression for $\tilde{c}_2$ [Eqs. (B13) and (B16)], the solvability condition for Eqs. (B19) and (B20) gives

$$\frac{-(6-\lambda_s^2)[Chi(\lambda_s)-Shi(\lambda_s)]e^{\lambda_s}\lambda_s^4}{8(\lambda_s^3+4\lambda_s^2+9\lambda_s+9)}$$

$$+\frac{(\lambda_s^2+2\lambda_s+2)(\lambda_s^3-3\lambda_s^2+6)}{8(\lambda_s^3+4\lambda_s^2+9\lambda_s+9)}$$

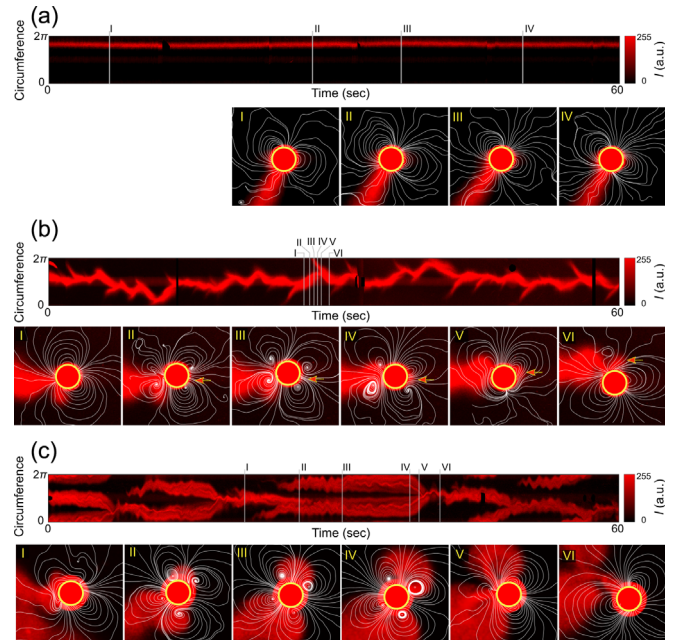$$=\frac{10}{\text{Pe}}\frac{(1+\mu)(1+3m)}{(2\mu+3)(1+5m)}. \qquad (B22)$$



FIG. 11. Additional data for Fig. 3: Kymographs of the chemical field with selected instantaneous frames. Rows (a), (b), and (c), respectively, correspond to Pe = 4, Pe = 36, and Pe = 293. In (b), the red arrow shows the location of the growing filled micelle blob.

Equations (B21) and (B22) are solved numerically to evaluate the variations of the nondimensional growth rates $[\lambda = (\lambda_s^2/\text{Pe})]$ with Pe for the first and second instability modes, respectively [Fig. 4(c) in the main text]. Note that Eq. (B21) is identical to that derived for the spontaneous motion of an autophoretic isotropic particle [23]. Furthermore, it is important to note here that the inverse

of the timescale used for nondimensionalizing the growth rate is $V_t/R_d$, which is consistent with the entire analysis.

## APPENDIX C: SUPPLEMENTAL FIGURES

Extending Fig. 3, Fig. 11 provides additional flow field snapshots to illustrate transient flow modes, with the
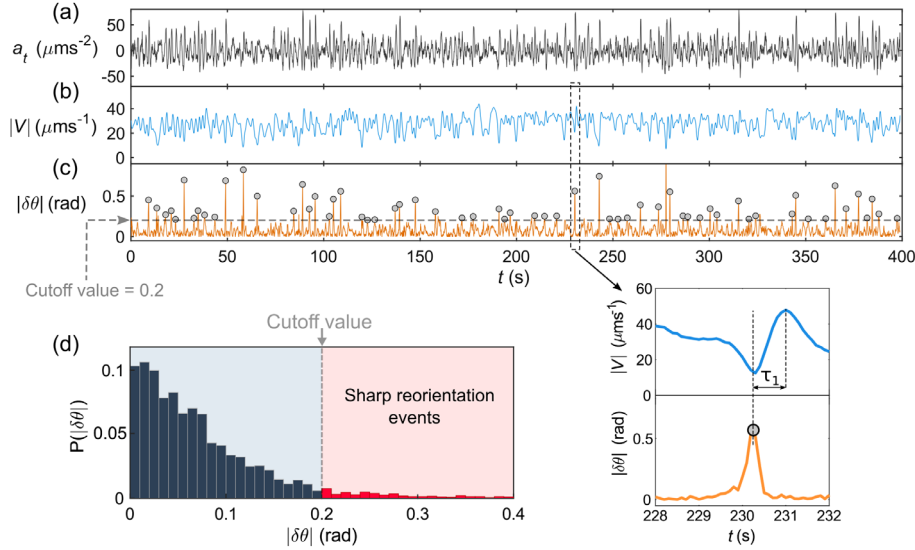


FIG. 12.    Conditional averaging over reorientation events. (a), (b), and (c) are tangential acceleration, speed, and the reorientation angle magnitude, respectively. In (c), the identified sharp reorientation events are shown by gray ($\circ$) symbols. The enlarged view is one example event that shows the general trend, a delay, $\tau_1$, between $|\delta\theta|$ and $|V|$. (d) The distribution of $|\delta\theta|$ and the cutoff value. The sharp turning events are colored in red.
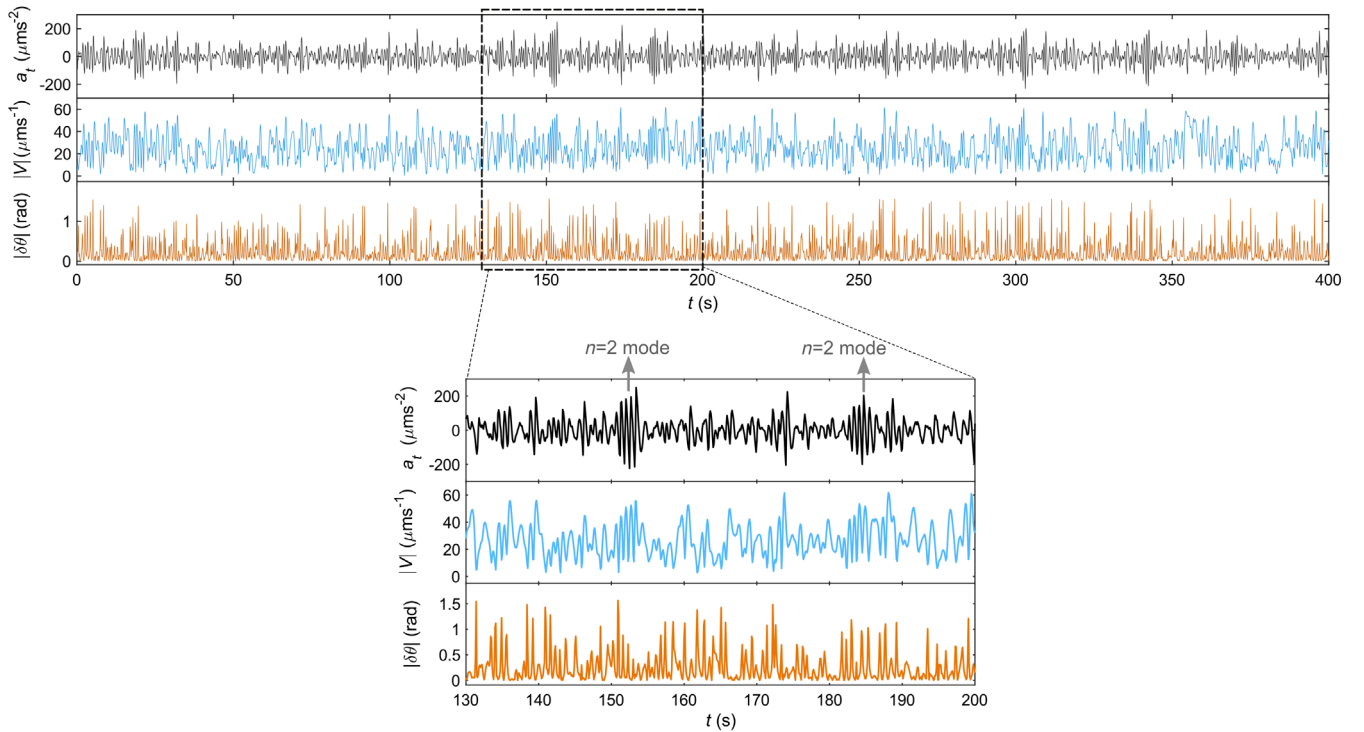


FIG. 13.    Signatures of bimodal space exploration in the long-time tangential acceleration signal. The corresponding Pe is 293.

chemical field kymographs plotted for a longer period of 60 s. Supporting Videos S6–S8, respectively, correspond to the kymographs in Figs. 11(a)–11(c).

In Fig. 12, we plot the long-time tangential acceleration, speed, and reorientation angle for Pe = 36. This dataset is used to identify the abrupt reorientation events. We identify these events based on a cutoff criterion for the reorientation between video frames $|\delta\theta| = 0.2$ rad [Figs. 12(c) and 12(d)], aligned and overlaid the profiles of all events with the turning point ($|\delta\theta_{max}|$) set as $t = 0$, and calculated the time-dependent average ($\langle\rangle$ represents ensemble averaging over all events).

In Fig. 13, we plot the long-time acceleration signal for Pe = 293 to demonstrate signatures of bimodal swimming. Such events can be identified by intermittent strong fluctuations in the acceleration profile. The enlarged view further demonstrates the difference between stopping ($n = 2$) and swimming modes ($n = 1$). Constant transitions between these modes result in the anomalous diffusive behavior shown in Fig. 6 in the main text.

---

[1] R. N. Bearon, *Helical Swimming Can Provide Robust Upwards Transport for Gravitactic Single-Cell Algae; a mechanistic model*, J. Math. Biol. **66**, 1341 (2013).

[2] M. Rossi, G. Cicconofri, A. Beran, G. Noselli, and A. DeSimone, *Kinematics of Flagellar Swimming in Euglena Gracilis: Helical Trajectories and Flagellar Shapes*, Proc. Natl. Acad. Sci. U.S.A. **114**, 13085 (2017).

[3] R. Stocker, *Reverse and Flick: Hybrid Locomotion in Bacteria*, Proc. Natl. Acad. Sci. U.S.A. **108**, 2635 (2011).

[4] L. Cisneros, C. Dombrowski, R. E. Goldstein, and J. O. Kessler, *Reversal of Bacterial Locomotion at an Obstacle*, Phys. Rev. E **73**, 030901(R) (2006).

[5] K. Y. Wan and R. E. Goldstein, *Time Irreversibility and Criticality in the Motility of a Flagellate Microorganism*, Phys. Rev. Lett. **121**, 058103 (2018).

[6] W. Gilpin, V. N. Prakash, and M. Prakash, *Vortex Arrays and Ciliary Tangles Underlie the Feeding–Swimming Trade-off in Starfish Larvae*, Nat. Phys. **13**, 380 (2017).

[7] A. C. H. Tsang, A. T. Lam, and I. H. Riedel-Kruse, *Polygonal Motion and Adaptable Phototaxis via Flagellar Beat Switching in the Microswimmer Euglena Gracilis*, Nat. Phys. **14**, 1216 (2018).

[8] K. Son, J. S. Guasto, and R. Stocker, *Bacteria Can Exploit a Flagellar Buckling Instability to Change Direction*, Nat. Phys. **9**, 494 (2013).

[9] A. J. T. M. Mathijssen, N. Figueroa-Morales, G. Junot, É. Clément, A. Lindner, and A. Zöttl, *Oscillatory Surface Rheotaxis of Swimming E. Coli Bacteria*, Nat. Commun. **10**, 3434 (2019).

[10] N. Figueroa-Morales, A. Rivera, R. Soto, A. Lindner, E. Altshuler, and É. Clément, *E. Coli "Super-contaminates" Narrow Ducts Fostered by Broad Run-Time Distribution*, Sci. Adv. **6**, eaay0155 (2020).

[11] G. H. Wadhams and J. P. Armitage, *Making Sense of It All: Bacterial Chemotaxis*, Nat. Rev. Mol. Cell Biol. **5**, 1024 (2004).

[12] E. P. Ipiña, S. Otte, R. Pontier-Bres, D. Czerucka, and F. Peruani, *Bacteria Display Optimal Transport near Surfaces*, Nat. Phys. **15**, 610 (2019).

[13] Ò. Guadayol, K. L. Thornton, and S. Humphries, *Cell Morphology Governs Directional Control in Swimming Bacteria*, Sci. Rep. **7**, 2061 (2017).

[14] J. Palacci, S. Sacanna, A. Abramian, J. Barral, K. Hanson, A. Y. Grosberg, D. J. Pine, and P. M. Chaikin, *Artificial Rheotaxis*, Sci. Adv. **1**, e1400214 (2015).

[15] J. Katuri, W. E. Uspal, J. Simmchen, A. Miguel-López, and S. Sánchez, *Cross-Stream Migration of Active Particles*, Sci. Adv. **4**, eaao1755 (2018).

[16] C. Jin, C. Krüger, and C. C. Maass, *Chemotaxis and Autochemotaxis of Self-Propelling Droplet Swimmers*, Proc. Natl. Acad. Sci. U.S.A. **114**, 5089 (2017).

[17] B. Liebchen and H. Löwen, *Synthetic Chemotaxis and Collective Behavior in Active Matter*, Acc. Chem. Res. **51**, 2982 (2018).

[18] B. ten Hagen, F. Kümmel, R. Wittkowski, D. Takagi, H. Löwen, and C. Bechinger, *Gravitaxis of Asymmetric Self-Propelled Colloidal Particles*, Nat. Commun. **5**, 4829 (2014).

[19] M. Suga, S. Suda, M. Ichikawa, and Y. Kimura, *Self-Propelled Motion Switching in Nematic Liquid Crystal Droplets in Aqueous Surfactant Solutions*, Phys. Rev. E **97**, 062703 (2018).

[20] A. Izzet, P. G. Moerman, P. Gross, J. Groenewold, A. D. Hollingsworth, J. Bibette, and J. Brujic, *Tunable Persistent Random Walk in Swimming Droplets*, Phys. Rev. X **10**, 021035 (2020).

[21] C. C. Maass, C. Krüger, S. Herminghaus, and C. Bahr, *Swimming Droplets*, Annu. Rev. Condens. Matter Phys. **7**, 171 (2016).

[22] S. Herminghaus, C. C. Maass, C. Krüger, S. Thutupalli, L. Goehring, and C. Bahr, *Interfacial Mechanisms in Active Emulsions*, Soft Matter **10**, 7008 (2014).

[23] S. Michelin, E. Lauga, and D. Bartolo, *Spontaneous Autophoretic Motion of Isotropic Particles*, Phys. Fluids **25**, 061701 (2013).

[24] Z. Izri, M. N. van der Linden, S. Michelin, and O. Dauchot, *Self-Propulsion of Pure Water Droplets by Spontaneous Marangoni-Stress-Driven Motion*, Phys. Rev. Lett. **113**, 248302 (2014).

[25] M. Morozov and S. Michelin, *Nonlinear Dynamics of a Chemically-Active Drop: From Steady to Chaotic Self-Propulsion*, J. Chem. Phys. **150**, 044110 (2019).

[26] M. Morozov and S. Michelin, *Self-Propulsion near the Onset of Marangoni Instability of Deformable Active Droplets*, J. Fluid Mech. **860**, 711 (2019).

[27] M. Morozov, *Adsorption Inhibition by Swollen Micelles May Cause Multistability in Active Droplets*, Soft Matter **16**, 5624 (2020).

[28] J. L. Anderson, *Colloid Transport by Interfacial Forces*, Annu. Rev. Fluid Mech. **21**, 61 (1989).

[29] See Supplemental Material at http://link.aps.org/supplemental/10.1103/PhysRevX.11.011043 for Supplemental Videos and their descriptions.

[30] T. Bhattacharjee and S. S. Datta, *Bacterial Hopping and Trapping in Porous Media*, Nat. Commun. **10**, 2075 (2019).

[31] W.-F. Hu, T.-S. Lin, S. Rafai, and C. Misbah, *Chaotic Swimming of Phoretic Particles*, Phys. Rev. Lett. **123**, 238004 (2019).

[32] L. G. Leal, *Advanced Transport Phenomena: Fluid Mechanics and Convective Transport Processes*, Cambridge Series in Chemical Engineering (Cambridge University Press, Cambridge, England, 2007).

[33] G. Slade, *Self-Avoiding Walks*, Math. Intell. **16**, 29 (1994).

[34] J. Najafi , M. R. Shaebani, T. John, F. Altegoer, G. Bange, and C. Wagner, *Flagellar Number Governs Bacterial Spreading and Transport Efficiency*, Sci. Adv. **4**, eaar6425 (2018).

[35] R. Golestanian, *Anomalous Diffusion of Symmetric and Asymmetric Active Colloids*, Phys. Rev. Lett. **102**, 188305 (2009).

[36] C. R. Reid, T. Latty, A. Dussutour, and M. Beekman, *Slime Mold Uses an Externalized Spatial Memory to Navigate in Complex Environments*, Proc. Natl. Acad. Sci. U.S.A. **109**, 17490 (2012).

[37] A. G. Cherstvy, O. Nagel, C. Beta, and R. Metzler, *Non-Gaussianity, Population Heterogeneity, and Transient Superdiffusion in the Spreading Dynamics of Amoeboid Cells*, Phys. Chem. Chem. Phys. **20**, 23034 (2018).

[38] B. V. Hokmabad, K. A. Baldwin, C. Krüger, C. Bahr, and C. C. Maass, *Topological Stabilization and Dynamics of Self-Propelling Nematic Shells*, Phys. Rev. Lett. **123**, 178003 (2019).

[39] M. Schmitt and H. Stark, *Swimming Active Droplet: A Theoretical Analysis*, Europhys. Lett. **101**, 44008 (2013).

[40] C. H. Meredith, P. G. Moerman, J. Groenewold, Yu.-J. Chiu, W. K. Kegel, A. van Blaaderen, and L,. D. Zarzar, *Predator–Prey Interactions between Droplets Driven by Non-reciprocal Oil Exchange*, Nat. Chem. **12**, 1136 (2020).

[41] M. Jabbarzadeh and H. C. Fu, *Viscous Constraints on Microorganism Approach and Interaction*, J. Fluid Mech. **851**, 715 (2018).

[42] B. Nasouri and R. Golestanian, *Exact Phoretic Interaction of Two Chemically Active Particles*, Phys. Rev. Lett. **124**, 168003 (2020).

[43] K. Lippera, M. Benzaquen, and S. Michelin, *Bouncing, Chasing, or Pausing: Asymmetric Collisions of Active Droplets*, Phys. Rev. Fluids **5**, 032201(R) (2020).

[44] F. Yang, B. Rallabandi, and H. A. Stone, *Autophoresis of Two Adsorbing/Desorbing Particles in an Electrolyte Solution*, J. Fluid Mech. **865**, 440 (2019).

[45] Y. Couder, S. Protière, E. Fort, and A. Boudaoud, *Walking and Orbiting Droplets*, Nature (London) **437**, 208 (2005).

[46] M. Hubert, S. Perrard, M. Labousse, N. Vandewalle, and Y. Couder, *Tunable Bimodal Explorations of Space from Memory-Driven Deterministic Dynamics*, Phys. Rev. E **100**, 032201 (2019).

[47] R. N. Valani, A. C. Slim, and T. Simula, *Superwalking Droplets*, Phys. Rev. Lett. **123**, 024503 (2019).

[48] J. Petit, I. Polenz, J.-C. Baret, S. Herminghaus, and O. Bäumchen, *Vesicles-on-a-Chip: A Universal Microfluidic Platform for the Assembly of Liposomes and Polymersomes*, Eur. Phys. J. E **39**, 59 (2016).

[49] W. Thielicke and E. Stamhuis, *PIVlab—Towards User-Friendly, Affordable and Accurate Digital Particle Image Velocimetry in MATLAB*, J. Open Res. Software **2**, e30 (2014).

[50] W. Gilpin, V. N. Prakash, and M. Prakash, *Flowtrace: Simple Visualization of Coherent Structures in Biological Fluid Flows*, J. Exp. Biol. **220**, 3411 (2017).